

Enhanced diffusion through porous nanoparticle optical multilayers

Carmen López-López ^a, Silvia Colodrero ^a, Sonia R. Raga ^b, Henrik Lindström ^c, Francisco Fabregat-Santiago ^b, Juan Bisquert ^b and Hernán Míguez ^a

^a Instituto de Ciencia de Materiales de Sevilla, Consejo Superior de Investigaciones Científicas-Universidad de Sevilla, Américo Vespucio 49, 41092, Sevilla, Spain. E-mail: hernan@icmse.csic.es

^b Departament de Física, Universitat Jaume I, Vicent Sos Baynat s/n, 12071, Castelló, Spain

^c NLAB Solar Laboratories, Drottning Kristinas väg 45, SE-114 28, Stockholm, Sweden

Herein we demonstrate improved mass transport through nanoparticle one-dimensional photonic crystals of enhanced porosity. Analysis is made by impedance spectroscopy using iodine and ionic liquid based electrolytes and shows that newly created large pores and increased porosity improve the diffusion of species through the photonic crystal. This achievement is based on the use of a polymeric porogen (polyethylene glycol), which is mixed with the precursor suspensions used for the deposition of nanoparticle TiO₂ and SiO₂ layers and then eliminated to generate a more open interconnected void network, as confirmed by specular reflectance porosimetry. A compromise between pore size and optical quality of these periodic structures is found.

Introduction

Recently, different variants of porous one-dimensional photonic crystals (1DPCs) have been proposed and built.^{1–12} To create these porous multilayers in which the dielectric constant varies periodically along one direction, numerous methods have been developed in the last few years, such as deposition of supramolecularly templated films,^{2,5} glancing angle vapor physical deposition,^{1,4,12} sol–gel,¹¹ or electrochemical etching.^{8,10} One of the most versatile techniques is the deposition of nanoparticle suspensions by spin or dip coating.^{3,6,7} Although these materials were first proposed by Thomas in the late eighties,¹³ and research on them continued in the nineties,¹⁴ it is now when the field is blooming and its technological potential is beginning to be explored.^{15,16} The added value of these latter optical multilayers relies on their interconnected porosity, which makes their inner void network accessible to melted or dissolved polymers,^{17,18} liquids or gases,¹⁹ as well as on their ease of design and their high versatility for deposition onto a wide diversity of substrates. Actually, these properties have boosted the exploration of applications in fields such as optical sensing^{20–22} or photovoltaic devices.²³ The first of these is based on the fact that these films show a

different structural color upon infiltration of different guest compounds into the porous network, which alters the effective refractive index of the structure. On the other hand, porous 1DPCs have also been employed as coherent mirrors to improve light harvesting efficiency in dye sensitized solar cells.²³ In this case, their porous mesostructure allows the electrolyte to soak the entire electrode, thus providing high reflectivity and allowing charge transport through the cell. All these applications are highly dependent on both the degree of porosity and the pore size distribution of the films.

Typically, higher dielectric contrast (i.e., wider and more intense Bragg reflections) is attained for multilayers built by alternate deposition of amorphous SiO₂ and nanocrystalline TiO₂. Up to now, the porosity of nanoparticle 1DPCs has only been controlled through both the degree of aggregation and the particle size of the precursor suspensions,^{6,17} which has even made it possible to build periodic multilayers of homogeneous composition.²⁴ However, the TiO₂ nanocrystalline particles typically employed give rise to layers of small pore size, which might impede the proper flow of species throughout the periodic multilayer, limiting their potential application in electrochemical devices.

Herein we demonstrate improved mass transport through nanoparticle 1DPCs of enhanced porosity. Analysis is made by impedance spectroscopy (IS) using iodine and ionic liquid based electrolytes. This achievement is based on the use of a polymeric porogen (polyethylene glycol), which is mixed with the precursor suspensions used for the deposition of the TiO₂ and SiO₂ layers and then eliminated to generate a more open interconnected void network. A similar method has recently been proposed to improve mass transport in photocatalytic films.²⁵ This allows controlling both the degree of porosity and the pore size distribution of TiO₂ (np-TiO₂) and SiO₂ nanoparticle (np-SiO₂) layers integrated in 1DPCs. We study the changes of the structural properties caused by the alteration of the pore structure in, first, monolayers made of TiO₂ nanocrystals and amorphous SiO₂ nanospheres and, then, in multilayers containing them. In spite of achieving a large increase in average pore size, the optical quality of the structure is preserved. A reduction of the electrolyte diffusion resistance of above 40% with respect to the starting multilayer is found. These results open the route to optimize the performance of photo-electro-chemical devices in which less porous optical multilayers have already been successfully integrated.

Experimental

Preparation of particle suspensions

The starting materials were suspensions of nanoparticles of SiO₂ and TiO₂. They were employed in the production of these multilayers due to the high refractive index contrast between them. SiO₂ nanocolloids (average size of 30 nm) were purchased from Dupont (LUDOX TMA, Aldrich), while TiO₂ nanocrystallites (average size of 10 nm) were synthesized using a variation of a method based on the hydrolysis of titanium tetraisopropoxide followed by a peptization process under hydrothermal conditions.²⁶ Titanium tetraisopropoxide (20 ml, 97% Aldrich) was added to Milli-Q water (36 ml) and stirred for 1 hour. Once the alkoxide was hydrolyzed, the product was filtered to collect the solid formed and washed several times with distilled water. Then, it was peptized in a Teflon reactor containing 3.9 ml of 0.6 M tetramethylammonium hydroxide ([similar]2.8 M, Fluka) at 120 °C for 3 h. Later centrifugation

at 14000 rpm for 10 minutes allows elimination of some large aggregates from the dispersion, the concentration of the resultant suspension being typically between 24 and 25 wt%. TiO₂ and SiO₂ nanoparticles are diluted to 5 and 2 wt% respectively, in a mixture of water, 21 vol%, and methanol, 79 vol%, in order to use as precursors for the spin-coating process. Prior to their deposition each suspension was ultrasonicated for several minutes to re-disperse aggregates.

The polymer chosen to alter the porous network is polyethylene glycol (PEG) because it exhibits good film forming properties, and reduces the density of defects present in the films made by spin-coating.¹⁷ The influence that the addition of different quantities of PEG to the TiO₂ and SiO₂ precursor suspensions has on the mesostructure of these nanoparticle Bragg reflectors was analyzed afterward. It should be mentioned that there are other methods that allow control of the porosity of nanocrystalline TiO₂ films, which involve the synthesis of particles within polyelectrolyte multilayers.²⁷ Also, the increase of particle size to enlarge the average pore size was discarded since it could give rise to unwanted diffuse scattering, as it has been proven before.²⁸

Preparation of monolayer and multilayer films

Both np-TiO₂ monolayers and np-SiO₂/np-TiO₂ stacks with 1DPC properties made of five bilayers were built by deposition of the diluted TiO₂ and SiO₂ nanoparticle suspensions by spin-coating (final speed $\omega = 5000$ rpm; acceleration $\gamma = 9180$ rpm⁻¹; time 60 s), followed by heat treatment in an oven at 450 °C for 30 min to provide the films with mechanical stability. In order to achieve the desired monolayer thickness, several depositions of the same precursor suspension were carried out. The substrates used to deposit monolayers and multilayers were silicon and glass, respectively. Both substrates were previously treated to enhance their hydrophilicity and, consequently, improve the first layer deposition. The films prepared presented high optical quality and displayed uniform color arising from the interference of the beams reflected by the different interphases.

In order to build the monolayers and multilayers using the np-SiO₂/PEG and the np-TiO₂/PEG precursor suspensions we also employed the spin coating protocol described above, although in this case it was necessary to perform a thermal annealing at 300 °C for 15 minutes in air after each deposition to eliminate the PEG from the structure and to consolidate the stacking of these layers. Without this intermediate treatment, it was not possible to create a new layer on top, since the deposited film did not adhere properly. Finally, the remaining polymer is eliminated after calcination of the whole multilayer at 450 °C for 1 hour in air.

Materials characterization

The new porous mesostructure of the TiO₂ and SiO₂ films was assessed by Specular Reflectance Porosimetry (SRP). This technique is based on the analysis of the shift of the optical response at equilibrium as the vapor pressure of a volatile liquid, first, gradually increases up to saturation and, then, decreases down to the initial value in a closed chamber. In this way, the adsorption-desorption isotherm curves of the np-TiO₂/PEG and the np-SiO₂/PEG monolayers were obtained. The solvent used to execute this study was isopropanol, which has proven to yield excellent results for the analysis of vapor sorption properties of

complex mesostructured and nanoparticle based multilayers.^{19,29,30} This technique allows us to obtain the effective refractive index of each one of the films and, by using the Bruggeman equation, analyze the evolution of both the overall porosity and the pore size distribution as the concentration of PEG in the precursor liquid varies. Analysis of the specular reflectance spectra obtained at normal incidence was performed by simulating and fitting the optical response measured at the different solvent partial pressures. To do so, we employed a code written in MatLab based on the transfer matrix method and that has been thoroughly described before.³¹ Reflectance spectra were attained using a Fourier transform spectrophotometer (Bruker IFS-66 FTIR) attached to a microscope and operating in reflection mode with a 4× objective with 0.1 of numerical aperture (light cone angle $\pm 5.7^\circ$). Please notice that the inadequacy of using standard BET techniques (based on sample weight changes caused by N₂ adsorption and desorption from the pore walls) for the study of porous mesostructured films arises from the too low weight of the films. On the other hand, ellipsometry relies on the use of one-side polished silicon wafers as substrates, which would largely affect their optical properties. The images of cross-section were acquired with a field-emission scanning electron microscope (FESEM , Hitachi S-4800 operating at 2 kV).

Impedance spectroscopy measurements

IS analysis was performed over cells containing a solution made with 0.13 M iodine in 1-butyl-3-methylimidazolium iodide. Each cell was composed of two platinized FTO electrodes , one of them with an np-SiO₂/np-TiO₂ multilayer, for which different quantities of PEG were employed, deposited over the Pt-coated glass. An area of 1 × 1 cm² was drawn over conductive glass leaving a 2 mm wide strip on one of the sides to evacuate the charge and make the contacts. FTO out of this area was removed via etching with Zn powder and diluted HCl. Then the electrodes were electroplatinized by submerging them into a diluted chloroplatinic acid aqueous solution using a Pt sheet as a counter-electrode and applying a potential of 1.5 V for 1 minute. After this process, dark FTO electrodes were obtained, indicating that a high concentration of Pt was deposited over the surface. The cells were mounted after drop casting the electrolyte in one of the electrodes and fixing the second by pressing it strongly with a clamp. Pressing electrodes together with a clamp ensures to reach a distance between electrodes equal to the photonic crystal thickness. The removal of external FTO avoids both short circuiting of the cells and direct diffusion of iodide between uncovered FTO layers, minimizing edge effects. The conductive strips of the opposed electrodes were oriented in contrary faces also to prevent short circuits. The iodine concentration used in the electrolyte is lower than that found in the literature because the short distance between electrodes makes it more difficult to reach the current saturation regime.³² Furthermore, a pure ionic liquid is necessary in this experiment both to avoid evaporation during measurements and to be able to appreciate the differences in diffusion due to porosity. Electrochemical measurements were carried out in this two electrode configuration and collected after letting the electrolyte penetrate into the pores of the nanoparticle 1DPC. First, a current–voltage curve between 0 and 1.5 V was made to measure the limiting currents reached. Then galvanostatic IS curves were attained taking 4 different currents starting from 0 mA to near the saturation current for each cell . Analysis of the parameters obtained at the same current density was performed in order to obtain comparable results between the different samples. IS data were fitted to a Randles circuit model.

Results and discussion

Analysis of pore size and porosity

The different degree of porosity extracted from the analysis of the specular reflectance spectra of the np-TiO₂/PEG and np-SiO₂/PEG layers in air is shown in Table 1. On the other hand, the change in the optical response of these porous layers versus the gradual increase or decrease of the vapor pressure of a liquid solvent provides us with information on the different pore size distribution. Adsorption–desorption isotherms are presented in Fig. 1 and 2. This analysis reveals that the starting (containing no polymer) np-SiO₂ layers present a much larger average pore size than np-TiO₂ ones and that the addition of PEG produces more significant changes in both the pore size and average porosity of the second kind of layers. Hence more effort was devoted to improve the pore network of the TiO₂ layer since the bottleneck for optimized electrolyte flow must be the narrowest pores of the multilayer, present in the np-TiO₂ layers.

First of all, as presented in Table 1, as the PEG[thin space (1/6-em)]:[thin space (1/6-em)]np-TiO₂ weight ratios increase from 0 to 0.75, the effective refractive index decreases from 1.70 to 1.50, which implies that the accessible porosity of these layers rises from 47% to 60%. In the case of SiO₂ films, the refractive index varies from an already low 1.25 to 1.22 when the PEG[thin space (1/6-em)]:[thin space (1/6-em)]np-SiO₂ weight ratio is 0.50, with the porosity changing from 44% to 50%.

Noteworthy, all adsorption–desorption isotherms measured can be classified as type IV_{33,34} following a standard classification of the capillary condensation response of mesoporous materials (pore size between 2 and 50 nm). In the curves attained from the np-TiO₂ layer (Fig. 1a), the volume of solvent infiltrated within the structure increases as the pressure goes up to a specific value of $P/P_0 = 0.93$, where P_0 is the saturation vapor pressure of isopropanol at room temperature, with the filled pore volume remaining constant for higher pressures. This fact indicates that the accessible porosity of the layer is completely filled with the solvent employed. However, this trend is not observed for the case of the isotherms measured from the layers in which the PEG was used to change their internal porous structure (Fig. 1b and c), which is in consonance with the expected effect of the porogen on the mesostructure, namely, the creation of large cavities in which condensation of the vapor is prevented. Pore size distributions of the different np-TiO₂ and np-TiO₂/PEG films were extracted from the isotherm data, as presented in Fig. 1d–f. The porous structure attained after spin coating the np-TiO₂ precursor suspension without PEG is a network of voids whose size is comprised between 4 nm and 18 nm. Broader pore radius ranges, up to 24 nm, are obtained when the different amounts of polymer are employed. For the case of films made of suspensions containing PEG[thin space (1/6-em)]:[thin space (1/6-em)]np-TiO₂ weight ratios of 0.25 and 0.50, the larger pore radius created cannot be estimated from the isotherm curves since the plateau at higher partial vapor pressures is not reached. Nevertheless, pore size distributions demonstrate that both the porosity and the pore size are largely increased when PEG is used as porogen.

Similarly, adsorption–desorption isotherms and pore size distributions of both np-SiO₂ and np-SiO₂/PEG layers are shown in Fig. 2. In this case, the most noteworthy difference is the increase of the radius of necks between nanoparticles of the sample when PEG is used, as it can be seen when Fig. 2c and d (grey circles and lines) are compared. Also, the pore size

distribution becomes wider and the average pore size shifts towards higher values. As expected, since layers formed by SiO₂ nanoparticles have larger pores than TiO₂ films to start with, the effect of porogen on the SiO₂ pore size is less noticeable, although in both types of layers the porosity rises with the concentration of porogen used in the precursor suspensions.

Highly porous layers in Bragg reflectors

Having demonstrated that both the porosity and the average pore size of np-TiO₂ and np-SiO₂ films are increased when PEG is added to the precursor suspensions, 1DPCs were built in order to prove that these new highly porous layers can also be integrated in a stack that presents photonic crystal properties. For that purpose, np-SiO₂ and np-TiO₂ precursor suspensions with different concentration of PEG were employed. FESEM images of cross-sections of multilayers made by alternating films deposited from these suspensions are shown in Fig. 3. The samples whose images are displayed were prepared using suspensions containing PEG[thin space (1/6-em)]:[thin space (1/6-em)]np-TiO₂ weight ratios of 0 (Fig. 3a) and 0.75 (Fig. 3b), while the same np-SiO₂ suspension containing no PEG was used for both samples.

The different pore structure of the TiO₂ layers can be clearly distinguished in these pictures. Furthermore, it can be readily observed that the thickness of the TiO₂ layer also increases with the PEG concentration in the precursor suspension, with thicknesses comprised between 60 nm and 130 nm being attained for PEG[thin space (1/6-em)]:[thin space (1/6-em)]np-TiO₂ weight ratios ranging from 0 to 0.75. The clear definition between the interfaces of np-TiO₂ and np-SiO₂ layers present in the originally made nanoparticle multilayers⁶ (Fig. 3a) fades when the polymer is used to modify the pore network (Fig. 3b) mainly due to the SiO₂ particle interpenetration within the large superficial pores of the TiO₂ layers. Long range uniformity is, however, preserved.

In the same way that it was done for the monolayers, the values of the effective refractive index and the porosity of each layer within the periodic stack were also estimated minimizing the difference between the simulated and the experimental reflectance spectra and using the Bruggeman equation, respectively. The results of the fittings are listed in Table 1. It can be noticed that the porosity of the np-TiO₂ layers remains practically unaltered after being integrated in the Bragg reflector when compared to that measured for monolayers. It should be remarked that control over the porosity of the films, like the one herein demonstrated, opens the possibility of designing the optical properties of the multilayers built with them with great precision, as it has actually been proven for other optical filters in which porosity, although not accessible, can be tailored to measure.³⁵ Also, we would like to remark that, although highly reflecting multilayers of controlled pore size distribution can be attained by supramolecular templating,³⁶ these cannot be easily integrated in photo-electro-chemical devices. This is due to the incompatibility of the compounds employed during the preparation of the supramolecularly templated mesostructure with the rest of materials present in the photocatalytic or photovoltaic cell : liquid phase precursors infiltrate the whole device, which yields the uncontrolled formation of metal oxide , drastically reducing the performance of the device. In contrast, when nanoparticle suspensions are used to form the multilayers, the solid phase is retained in the regions onto which it is deposited, while the liquid one evaporates or is easily removed by thermal annealing .

1DPCs of different porosity having their Bragg peaks in the same spectral range were built in order to study the influence that the new pore network structure may have on the control of the photonic crystal properties. This requires that all samples present the same unit cell optical thickness, $d_{uc} = (n_1t_1 + n_2t_2)$, being n_i and t_i the refractive index and the thickness of each type of layer present in the ensemble, since, in a first approximation, the Bragg peak is centred at $\lambda_B = 2d_{uc}$. This condition is achieved by modifying the concentrations of TiO₂ and SiO₂ precursor suspensions, since, as shown in Fig. 3, the actual thickness of a layer increases when the same concentrations of nanoparticles are mixed with increasing amounts of PEG. The specular reflectance spectra of these samples are displayed in Fig. 4. The comparison between the different spectra reveals that the presence of larger pores does not affect adversely the performance of the multilayers as Bragg reflectors. In all cases, the number of layers deposited is similar ($N = 10$) and primary maxima present intensities above 80%. Slightly higher peaks are achieved for 1DPCs in which the pores are finer. The reason for this effect is the lower refractive index contrast existing between the layers of np-TiO₂ and np-SiO₂ in those multilayers showing enhanced porosity, which diminishes the scattering strength of the lattice. Also, a clear narrowing of the peak spectral width is observed as the porosity increases. The photonic gap to midgap ratio, $\Delta\omega/\omega_0$, decreases from 25% in the original nanoparticle 1DPC to 20% in those with higher porosity. In fact, it can be shown that $\Delta\omega/\omega_0$ depends on the dielectric contrast, $\Delta n = |n_1 - n_2|$, like $\Delta\omega/\omega_0 = 2/\pi \Delta n/n$,³⁷ where n is the average refractive index, estimated as $n = (n_1t_1 + n_2t_2)/(t_1 + t_2)$. The generation of a more open pore network yields both lower Δn and n , as it can be estimated from the data shown in Table 1, and thus may lead to spectrally thinner Bragg reflections.

Enhanced diffusion through Bragg reflectors

To assess the effect that the modified pore network of 1DPCs has on mass transport, curves of current density vs. potential (j - V curves) and impedance spectroscopy measurements were performed over 1DPC samples immersed in a viscous electrolyte, 0.13 M of iodine in 1-butyl-3-methylimidazolium iodide, as schematized in Fig. 5a. As shown in Fig. 5b, the increase of the layer porosity and pore size with the addition of PEG produces a rise both in the slope at low potentials and in the value of the limiting current (j_{lim}) plateau (Fig. 5c) of the j - V curves. These results prove the enhancement of mass transport of an electrolyte embedded in 1DPC as a result of the control of porosity

For a more detailed analysis of these results, each sample was measured by impedance spectroscopy at four different currents between 0 mA and the limiting current. The typical impedance spectrum obtained from the porous 1DPC shown in Fig. 6a was fitted with the Randles equivalent circuit schematized in Fig. 6b. It allows analyzing separately the physical processes of carrier transport and charge transfer that take place in our device where R_s corresponds to the sum of the resistances associated with FTO, contacts and wires, R_{Pt} and C_{Pt} are the charge-transfer resistance and double-layer capacitance from the platinized electrodes, respectively, and Z_d is the diffusion impedance, which represents the resistance to mass transfer through the porous structure. From the expression of Z_d given by eqn (1), where

ω_d is the characteristic diffusion frequency, ω is the frequency of the measurement and i is the imaginary unit,

$$Z_d = R_d \frac{\tanh\left[(i\omega/\omega_d)^{1/2}\right]}{(i\omega/\omega_d)^{1/2}}$$

we obtain R_d , which is the resistance associated with diffusion of triiodide ions in the electrolyte and is the parameter that will be more affected by variations of the pore network in the multilayers.

From the diffusion frequency and film thickness, L , the diffusion coefficient may be obtained using $D = \omega_d L^2$ that yielded values comprised between 1.5 and $2.5 \times 10^{-8} \text{ cm}^2 \text{ s}^{-1}$, in good agreement with data obtained from j_{lim} calculations.³⁸ These values are one order of magnitude lower than those obtained in the free electrolyte,³² indicating certain difficulties in the transport of I_3^- through the 1DPC. We associate these low values of D with the increased tortuosity and constrictivity introduced by the 1DPC relative to the free electrolyte.

In practical terms, the diffusion resistance is the most relevant parameter of Z_d since its value determines, together with R_s and R_{Pt} , the total series resistance of the device. Thus it may influence its performance, mainly through the loss of fill factor, but eventually also by a drop in short circuit current.^{39,40} We thus focus our study on R_d in what follows.

Fig. 7a displays R_d as obtained from the analysis of the impedance spectra measured at several current densities, j . The different symbols (lines are just guides for the eye) correspond to photonic crystals possessing different pore networks. In all cases, R_d increases as the current does, reaching rather large values when j_{lim} is approached. It can be readily seen from Fig. 7a that samples with higher porosity present lower diffusion resistance, reaching values similar to those commonly found in optimized devices for R_s ($1-5 \text{ } \Omega \text{ cm}^2$) and R_{Pt} ($1-3 \text{ } \Omega \text{ cm}^2$).⁴⁰⁻⁴³ Fig. 7b clearly shows the dependence of R_d measured at 0 mA versus the average porosity within the multilayer structure. Again a clear decay of R_d as porosity is increased can be observed while, consequently, the opposite trend is observed for j_{lim} , as shown in Fig. 5c. It should also be noticed that this enhanced mass transport must be caused by the combined effect of both larger porosity and average pore size. However, these two effects cannot be analyzed separately: each time porosity is increased (see Table 1), the bottlenecks, responsible for the hindering of diffusion, are also enlarged (see Fig. 1d-f), thus also contributing to a better flow of species through the multilayer.

Impedance spectroscopy analysis confirms that multilayers built using mixtures of nanoparticles and PEG always present larger effective sections for the diffusion of I_3^- species, which results in lower diffusion resistances. This result, combined with the use of optimized electrolytes, allows beating the limitations to efficiency introduced by the addition of the 1DPC extra layers in photo-electro-chemical devices such as dye sensitized solar cells.^{23,44}

Conclusions

In summary, we have presented a method to enhance the mass transport through nanoparticle multilayers displaying one-dimensional photonic crystal properties. Addition of a

polymer in the precursor suspensions allows tuning the pore size distribution of the ensemble. Monolayers built from these suspensions have been analyzed by specular reflectance porosimetry to demonstrate that both the total accessible void volume and the average pore size of the film are increased. Stacks of these highly porous layers display intense Bragg reflections as well as improved mass transport , as confirmed by the diffusion resistance obtained for an electrolyte embedded in the structure from impedance spectroscopy measurements. These materials presenting combined optical and transport properties will give rise to improved performance when integrated into photo-electro-chemical devices.

Acknowledgements

HM thanks the Spanish Ministry of Science and Innovation for funding provided under grants MAT2008-02166 and MAT2011-23593, as well as Junta de Andalucía for grants FQM3579 and FQM5247. HM and JB thank project CONSOLIDER HOPE CSD2007-00007 for funding. UJI team also acknowledges financial support from the Spanish Ministry of Science and Innovation under project MAT2010-19827 and Generalitat Valenciana under project PROMETEO 2009/058.

Notes and references

1. J. J. Steele, A. C. van Popta, M. M. Hawkeye, J. C. Sit and M. J. Brett, *Sens. Actuators, B*, 2006, 120, 213
2. S. Y. Choi, M. Mamak, G. von Freymann, N. Chopra and G. A. Ozin, *Nano Lett.*, 2006, 6, 2456
3. Z. Wu, D. Lee, M. F. Rubner and R. E. Cohen, *Small*, 2007, 3, 1445
4. M. F. Schubert, J. Q. Xi, J. K. Kim and E. F. Schubert, *Appl. Phys. Lett.*, 2007, 90, 141115
5. M. C. Fuertes, F. J. Lopez-Alcaraz, M. C. Marchi, H. E. Troiani, V. Luca, H. Míguez and G. J. D. A. Soler-Illia, *Adv. Funct. Mater.*, 2007, 17, 1247
6. S. Colodrero, M. Ocaña and H. Míguez, *Langmuir*, 2008, 24, 4430
7. T. Druffel, N. Mandazy, M. Sunkara and E. Grulke, *Small*, 2008, 4, 459
8. D. L. Guo, L. X. Fan, F. H. Wang, S. Y. Huang and X. W. Zou, *J. Phys. Chem. C*, 2008, 112, 17952
9. B. V. Lotsch and G. A. Ozin, *Adv. Mater.*, 2008, 20, 4079
10. K. A. Killian, T. Böcking and J. J. Gooding, *Chem. Commun.*, 2009, 630
11. P. W. de Oliveira, C. Becker-Willinger and M. H. Jilavi, *Adv. Eng. Mater.*, 2010, 12, 349
12. L. González García, G. Lozano, A. Barranco, H. Míguez and A. R. Gonzalez-Elipse, *J. Mater. Chem.*, 2010, 20, 6408
13. I. M. Thomas, *Thin Solid Films*, 1989, 175, 173
14. M. Mennig, P. W. Oliveira, A. Frantzen and H. Schmidt, *Thin Solid Films*, 1999, 351, 225
15. O. Sánchez-Sobrado, M. E. Calvo and H. Míguez, *J. Mater. Chem.*, 2010, 20, 8240
16. P. Kurt, D. Banerjee, R. E. Cohen and M. F. Rubner, *J. Mater. Chem.*, 2009, 19, 8920
17. D. P. Puzzo, L. D. Bonifacio, J. Oreopoulos, C. M. Yip, I. Manners and G. A. Ozin, *J. Mater. Chem.*, 2009, 19, 3500
18. M. E. Calvo and H. Míguez, *Chem. Mater.*, 2010, 22, 3909
19. S. Colodrero, M. Ocaña, A. R. González-Elipse and H. Míguez, *Langmuir*, 2008, 24, 9135
20. O. Sánchez-Sobrado, M. E. Calvo, N. Núñez, M. Ocaña, G. Lozano and H. Míguez, *Nanoscale*, 2010, 2, 936
21. L. D. Bonifacio, D. P. Puzzo, S. Breslav, B. M. Willey, A. McGeer and G. A. Ozin, *Adv. Mater.*, 2010, 22, 1351
22. Z. H. Wang, J. H. Zhang, J. X. Li, J. Xie, Y. F. Li, S. Liang, Z. C. Tian, C. A. Li, Z. Y. Wang, T. Q. Wang, H. Zhang and B. Yang, *J. Mater. Chem.*, 2011, 21, 1264

23. S. Colodrero, A. Mihi, L. Haggman, M. Ocaña, G. Boschloo, A. Hagfeldt and H. Míguez, *Adv. Mater.*, 2008, 20, 1
24. M. E. Calvo, S. Colodrero, T. C. Rojas, J. A. Anta, M. Ocaña and H. Míguez, *Adv. Funct. Mater.*, 2008, 18, 2708
25. E. Della Gaspera, A. Antonello, M. Guglielmi, M. L. Post, V. Bello, G. Mattei, F. Romanato and A. Martucci, *J. Mater. Chem.*, 2011, 21, 4293
26. S. D. Burnside, V. Shklover, C. Barbé and K. Comte, et al. , *Chem. Mater.*, 1998, 10, 2419
27. M. Logar, B. Jancar and D. Suvorov, *J. Am. Ceram. Soc.*, 2010, 93, 3679
28. T. Druffel, O. Buazza, M. Lattis, S. Farmer, M. Spencer, N. Mandzy and E. A. Grulke, *Proc. SPIE–Int. Soc. Opt. Eng.*, 2008, 7030, 300
29. M. C. Fuertes, S. Colodrero, G. Lozano and A. Rodríguez González-Elipe, et al. , *J. Phys. Chem. C*, 2008, 112, 3157
30. F. Casanova, C. E. Chiang, C. P. Li, I. V. Roshchin, A. M. Ruminski, M. J. Sailor and I. K. Schuller, *Nanotechnology*, 2008, 19, 315709
31. G. Lozano, S. Colodrero, O. Caulier, M. E. Calvo and H. Míguez, *J. Phys. Chem. C*, 2010, 114, 3681
32. F. Fabregat-Santiago, J. Bisquert, E. Palomares, L. Otero, D. Kuang, S. M. Zakeeruddin and M. Grätzel, *J. Phys. Chem. C*, 2007, 111, 6550
33. S. Brunauer, L. S. Deming, W. S. Deming and E. Teller, *J. Am. Chem. Soc.*, 1940, 62, 1723
34. S. J. Gregg and K. S. W. Sing, *Adsorption, Surface Area and Porosity*, Academic Press, London, ISBN 0-12-300956-1, 1982
35. D. P. Partlow and T. W. O'Keeffe, *Appl. Opt.*, 1990, 29, 1526
36. N. Hidalgo, M. E. Calvo, M. Bellino, G. J. A. A. Soler-Illia and H. Míguez, *Adv. Funct. Mater.*, 2011, 21, 2534
37. A. Yariv and P. Yeh, *Optical Waves in Crystals*, John Wiley and Sons Inc., ISBN 0-471-43081-1, 2003
38. A. Hauch and A. Georg, *Electrochim. Acta*, 2001, 46, 3457
39. F. Fabregat-Santiago, J. Bisquert, G. Garcia-Belmonte, G. Boschloo and A. Hagfeldt, *Sol. Energy Mater. Sol. Cells*, 2005, 87, 117
40. F. Fabregat-Santiago, G. Garcia-Belmonte, I. Mora-Seró and J. Bisquert, *Phys. Chem. Chem. Phys.*, 2011, 13, 9083
41. T. Hoshikawa, M. Yamada, R. Kikuchi and K. Eguchi, *J. Electrochem. Soc.*, 2005, 152, E68

42. Y. Chiba, A. Islam, Y. Watanabe, R. Komiya, N. Koide and L. Han, *Jpn. J. Appl. Phys.*, 2006, 45, L638
43. J. Liu, R. Li, X. Si, D. Zhou, Y. Shi, Y. Wang, X. Jing and P. Wang, *Energy Environ. Sci.*, 2010, 3, 1924
44. S. Colodrero, A. Forneli, C. López-López, L. Pelleja, H. Míguez and E. Palomares, *Adv. Funct. Mater.*, 2011 DOI:10.1002/adfm.201102159 .

Figure captions

Figure 1. Adsorption (black circles and lines) and desorption (grey circles and lines) isotherms and pore size distribution measured by specular reflectance porosimetry from uniform monolayers made of (a and d) np-TiO₂ and np-TiO₂/PEG mixtures in which the weight ratio between the porogen and the nanoparticles is (b and e) 25% and (c and f) 50%.

Figure 2. Adsorption (black circles and lines) and desorption (grey circles and lines) isotherms and pore size distribution measured by specular reflectance porosimetry from uniform monolayers made of (a and c) np-SiO₂ and (b and d) np-SiO₂/PEG mixtures in which the weight ratio between the porogen and the nanoparticles is 50%.

Figure 3. FESEM images of cross-sections corresponding to Bragg reflectors made of alternate layers of spherical silica particles and titania nanocrystals. The latter was mixed with PEG in weight relations of (a) 0% and (b) 75% with respect to the weight of np-TiO₂ in the precursor suspension.

Figure 4. Specular reflectance spectra of 1DPCs in which different weight ratios of PEG were added to the precursor suspensions, namely, 0% (black solid line), 25% in TiO₂ (grey dashed line), 50% in TiO₂ (grey dotted line), 75% in TiO₂ (grey dashed-dotted line) and 50% in TiO₂/50% in SiO₂ (light grey solid line) with respect to that of nanoparticles.

Figure 5. (a) Scheme of the sandwich cells measured in this study. (b) j - V curves for the 1DPCs prepared from precursor suspensions containing different amounts of PEG in the np-TiO₂ layer: weight ratios of 0 (black solid line), 0.25 (dashed line), 0.5 (dotted line), and 0.75 (dashed-dotted line) while keeping the PEG[thin space (1/6-em)]:[thin space (1/6-em)]np-SiO₂ weight ratio constant and equal to 0. Results for a sample made using both PEG[thin space (1/6-em)]:[thin space (1/6-em)]np-TiO₂ and PEG[thin space (1/6-em)]:[thin space (1/6-em)]np-SiO₂ weight ratios of 0.5 are also shown (solid grey line) and (c) limit current obtained by extrapolating the values of the plateau on j - V curves versus average porosity of the multilayer.

Figure 6. (a) Impedance spectrum of a device made by sandwiching a photonic crystal and the electrolyte solution between two platinized electrodes. Galvanostatic measurement was performed at 10 mA over a sample made with 25% PEG in np-TiO₂. (b) Randles circuit used to fit experimental data.

Figure 7. (a) Diffusion resistance (R_d) versus current density (j) as extracted from the impedance spectroscopy analysis. (b) Diffusion resistance obtained at $j = 0$ mA cm⁻² versus average porosity of the 1DPC prepared using different PEG[thin space (1/6-em)]:[thin space (1/6-em)]np-TiO₂ weight ratios, namely, 0 (squares), 0.25 (circles), 0.5 (triangles), 0.75 (rhombus). Data for the multilayer prepared using both PEG[thin space (1/6-em)]:[thin space (1/6-em)]np-TiO₂ and PEG[thin space (1/6-em)]:[thin space (1/6-em)]np-SiO₂ weight ratios of 0.5 are also shown (stars).

Table 1

Table 1 Refractive index and porosity of the different nanoparticle monolayers and multilayers, as estimated from the analysis of the optical reflectance

Material	PEG/np (wt%)	n_{eff} monolayer	Porosity of monolayer (%)	n_{eff} of np-film in multilayer	Porosity of np-film in multilayer (%)
TiO ₂	—	1.70	47	1.69	47
	25	1.58	55	1.59	54
	50	1.55	57	1.54	57
	75	1.49	60	1.49	60
SiO ₂	—	1.25	44	1.27	42
	50	1.22	50	1.22	50

Figure 1

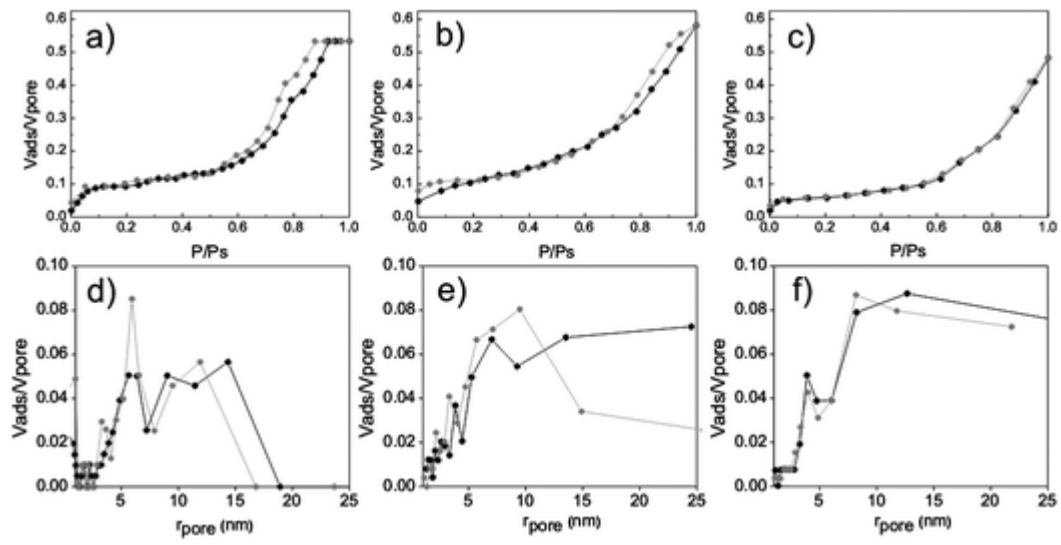


Figure 2

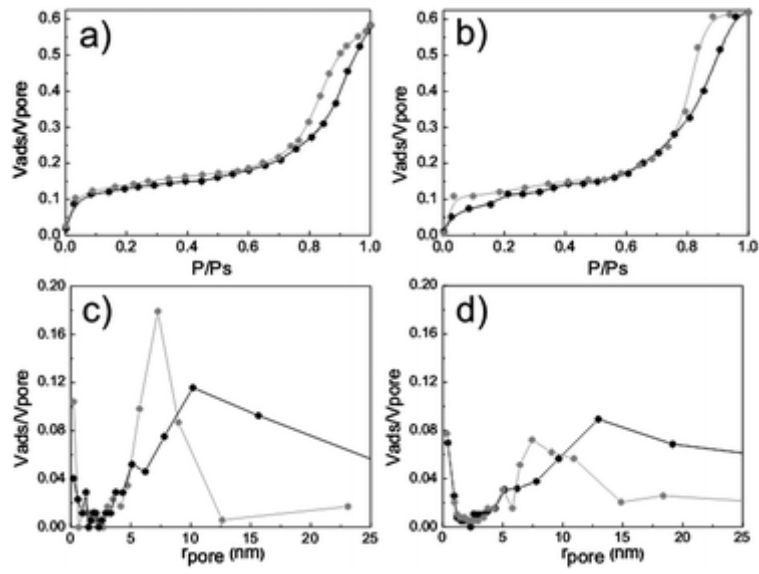


Figure 3

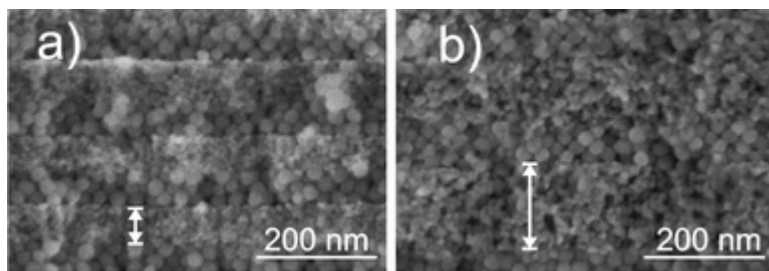


Figure 4

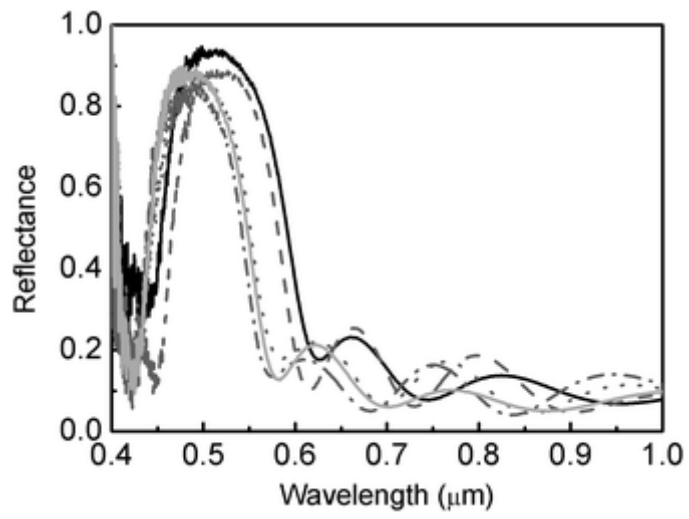


Figure 5

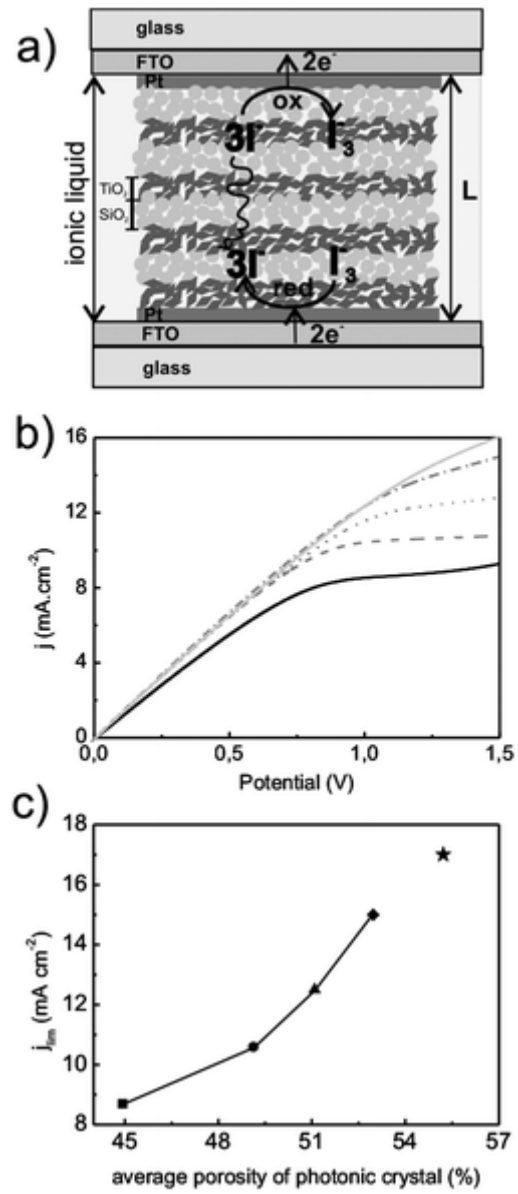


Figure 6

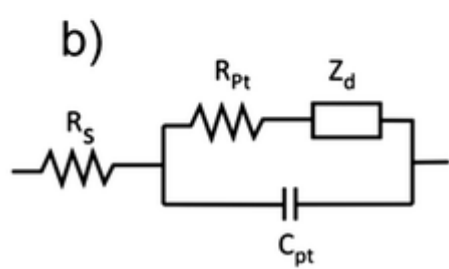
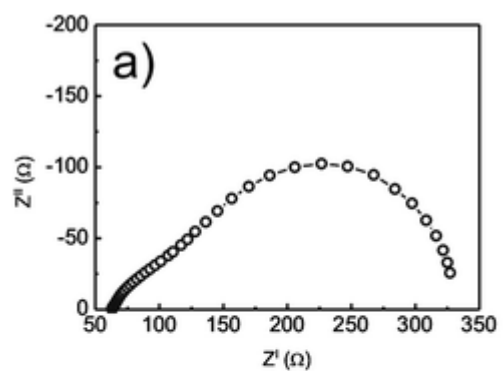


Figure 7

